Determination of the Rate Constant for the $NH_2(X^2B_1)$ + $NH_2(X^2B_1)$ Reaction at Low Pressure and 293 K

Mi-Kyung Bahng[†] and R. Glen Macdonald*

Chemical Sciences and Engineering Division, Argonne National Laboratory, 9700 South Cass Avenue, Argonne, Illinois 60439-4831

The rate constant for the reaction $NH_2(X^2B_1)$ + $NH_2(X^2B_1)$ → products was measured in CF_4, N_2 and Ar carrier gases at 293 ± 2 K over a pressure range from 2 to 10 Torr. The NH_2 radical was produced by the 193 nm photolysis of NH_3 dilute in the carrier gas. Both the loss of NH_3 and its subsequent recovery and the production of NH_2 and subsequent reaction were monitored simultaneously following the photolysis laser pulse. Both species were detected using quantitative time-resolved high-resolution absorption spectroscopy. The NH_3 molecule was monitored in the NIR using a rotation transition of the $\nu_1 + \nu_3$ first combination band near 1500 nm, and the NH_2 radical was monitored using the $^12_{21} \leftarrow {}^13_{31}$ rotational transition of the $(0,7,0)A^2A_1 \leftarrow (0,0,0) X^2B_1$ band near 675 nm. The low-pressure rate constant showed a linear dependence on pressure. The slope of the pressure dependence was dominated by a recombination rate constant for $NH_2 + NH_2$ given by $(8.0 \pm 0.5) \times 10^{-29}$, $(5.7 \pm 0.7) \times 10^{-29}$, and $(3.9 \pm 0.4) \times 10^{-29}$ cm^6 molecule^{-2} s^{-1} in CF_4, N_2, and Ar bath gases, respectively, where the uncertainties are $\pm2\sigma$ in the scatter of the measurements. The average of the three independent measurements of the sum of the disproportionation rate constants (the zero pressure rate constant) was $(3.4 \pm 6) \times 10^{-13}$ cm^3 molecule^{-1} s^{-1}, where the uncertainty is $\pm2\sigma$ in the scatter of the measurements.

I. Introduction

The amidogen radical, NH_2, plays an important role in combustion chemistry.[1] The most significant reaction[2] of NH_2 is the multichannel reaction with NO in which the dominant channel products are N_2 and H_2O, converting a major pollutant, NO, into N_2. On the other hand, the secondary channel, producing N_2 + H + OH, generates enough chain carriers, H and OH, under appropriate conditions to sustain the oxidation of an additive, usually NH_3. Several major NO_X abatement processes are based on this reaction. The thermal deNO$_X$ and NO$_X$OUT processes use the addition of NH_3 and $(NH_2)_2CO$, respectively, to remove NO_X from combustion exhaust gas streams.[3] The devolatilization of fuel-fixed nitrogen as HCN and NH_3 is a major source of NO_X pollutants in combustion. With the increased use of biomass fuels and their larger nitrogen content than coal or hydrocarbon fuels, the combustion chemistry of NH_3 will become a more important issue.[4]

The pyrolysis and combustion chemistry of both NH_3 and N_2H_4 have received renewed interest and detailed chemical models simulating their chemistry have raised important issues about our understanding of these processes.[5,6] Reactions involved in the high temperature pyrolysis of NH_3 have been discussed by Davidson et al.[7] At lower combustion temperatures, Allen et al.[8] showed that N_2H_x and NH_x species can be important even when simple fuels interact with nitrogen containing compounds such as N_2O. However, many of the reactions involving the NH_2 radical, especially those involving other transient species are not well characterized.[2] A recent study[9] of the low temperature oxidation chemistry of NH_3 detailed a complete

reaction mechanism describing this system, and illustrated the sensitivity of the system to either the generation of NO or N_2. The oxidation chemistry of NH_3 is also important in atmospheric chemistry;[10] however, the important atmospheric reactions of the NH_2 radical are similar to those in combustion chemistry, involving reactions with transient atmospheric species such as NO_2, NO, and HO_2.

In the present work, the rate constant for reaction 1, k_1, the self-reaction of $NH_2(X^2B_1)$,

$$NH_2 + NH_2 \rightarrow NH(X^3\Sigma^-) + NH_3 \qquad (1a)$$
$$\rightarrow NNH_2 + H_2 \qquad (1b)$$
$$\rightarrow N_2H_2(cis) + H_2 \qquad (1c)$$
$$\rightarrow N_2H_2(trans) + H_2 \qquad (1d)$$
$$\xrightarrow{[M]} N_2H_4 + M \qquad (1e)$$
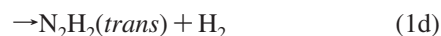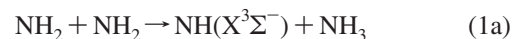
was measured at 293 K in a low-pressure regime where three-body recombination dominates the falloff kinetics. Reaction 1 is a radical–radical reaction where the interaction is characterized by two potential energy surfaces (PESs) of $^{3,1}A'$ electronic symmetry. Reaction 1a occurs on the triplet PES and the other channels on the singlet PES. At room temperature, Dransfeld et al.[11] experimentally established an upper limit of k_{1a} to be 3.0×10^{-15} cm^3 molecule^{-1} s^{-1}. At temperatures above 2000 K, Davidson et al.[7] found this channel to dominate. Theoretical calculations[12] of k_{1a} support the relatively high activation barrier for this reaction determined by these workers. The disproportionation reactions, 1b–1d, and the recombination reaction 1e, have only been investigated between temperatures of 300 and 500 K.

* To whom correspondence should be addressed. Fax: (630) 252-9292. E-mail: rgmacdonald@anl.gov.
† Current address: National Renewable Energy Laboratory, National Bioenergy Center, 1617 Cole Blvd., Golden, CO 80401.

NH$_2$(X^{2}B$_1$) + NH$_2$(X^{2}B$_1$) Reaction

J. Phys. Chem. A, Vol. 112, No. 51, 2008 **13433**

Reaction 1 has been studied by a variety of techniques to both initiate the reaction and monitor the NH$_2$ concentration; however, there is considerable uncertainty in the rate constant measurements describing this system. Gordon et al.[13] used pulse radiolysis of NH$_3$ to create the NH$_2$ radical and kinetic absorption spectroscopy to monitor its temporal concentration over the pressure range from 250 to 1520 Torr. Khe et al.[14] used flash photolysis of NH$_3$ dilute in N$_2$ and Ar and monitored NH$_2$ using kinetic absorption spectroscopy, and studied reaction 1 over the pressure range of 0.3 to 1000 Torr and temperatures between 300 and 500 K. At low pressures falloff effects are small and the reaction rate can be approximated by the sum of all the disproportionation rate constants, $k_1^0 = k_{1a} + k_{1b} + k_{1c} + k_{1d}$ and the three-body recombination rate, $k_{1e,0}$[M], where [M] is the concentration of the third body. These workers provided estimates of k_1^0 and $k_{1e,0}$ in NH$_3$, N$_2$, and Ar. The high-pressure limiting rate constant, $k_{1e,\infty}$, obtained by these workers was substantially smaller than the value obtained by Gordon et al.[13] Lozovskii et al.[15] used flash photolysis of NH$_3$ dilute in N$_2$ and Ar and intracavity laser absorption spectroscopy to measure the NH$_2$ concentration at given delay times from the initiating flash. These workers found k$_{1e,0}$ values for N$_2$ and Ar in agreement with Khe et al.[14] but a higher value for $k_{1e,\infty}$. Patrick and Golden[16] used 248 nm laser photolysis of O$_3$ to initiate reaction 1 following the O(^{1}D) + NH$_3$ reaction in O$_3$/NH$_3$/N$_2$ mixtures and high-resolution time-resolved laser-absorption spectroscopy to monitor NH$_2$ as a function of temperature at 200 Torr total pressure. Their measurements were in agreement with Khe et al.[14] at the same total pressure. Fagerström et al.[17] used pulsed radiolysis of NH$_3$ dilute in SF$_6$ and kinetic absorption spectroscopy to monitor the NH$_2$ concentration to study reaction 1a as a function of temperature from 300 to 500 K and a pressure range from 150 to 760 Torr. These workers used a Troe falloff analysis[18] of their own and a selection of previous data to extract broadening factors, F_{cent}, and limiting rate constants for high pressure, $k_{1e,\infty}$ and low pressure, k_{1e} conditions in four collision partners, NH$_3$, SF$_6$, N$_2$, and Ar. This analysis gave values of $k_{1e,0}$ for N$_2$ and Ar a factor of 2 larger than found by Khe et al.[14] The analysis of Fagerström et al.[17] has apparently reconciled the disagreement among the various works about the correct value for $k_{1e,\infty}$. Stothard et al.[19] used a fast flow discharge technique in F/NH$_3$/He and mass spectrometry detection to study the disproportionation channels at 300 K. They observed a mass 30 product from reactions 1b-1d at 0.5 and 0.75 Torr pressure, but followed the reaction by monitoring the decay of NH$_2$. Their k_1^0 value was similar to Khe et al.[14]'s value.

All previous studies of reaction 1 relied on some indirect method to calibrate the observed NH$_2$ absorption signals into an absolute concentration measurement. In particular, Khe et al.[14] used H atom scavenging by isobutane to generate H$_2$, and measured the concentration of H$_2$ by mass spectrometry following 100 photolysis flashes. They also used the decrease in the rate of the NH$_2$ + NO reaction following successive photolysis flashes as the NO was consumed in the subsequent chemistry to calibrate the initial NH$_2$ absorption signal. Both methods gave similar values for the NH$_2$ absorption coefficient.

In the current work, reaction 1 was studied in the low-pressure regime, 2 to 10 Torr, in dilute NH$_3$ mixtures in CF$_4$, N$_2$, or Ar to determine k_1^0, and $k_{1e,0}$ in each gas at 293 K. The reaction was initiated by 193 nm excimer laser photolysis of NH$_3$ to generate NH$_2$ and an H atom. Both temporal concentration profiles of NH$_3$ and NH$_2$ were simultaneously monitored by high-resolution, time-resolved, laser-absorption spectroscopy following the photolysis laser pulse. The initial loss of NH$_3$ was assumed equal to the initial production of NH$_2$ in order to calculate the peak absorption coefficient of NH$_2$. Ammonia was detected using a rotational transition of the $\nu_1 + \nu_3$ combination band near 1500 nm, and NH$_2$ was detected on the $^1 2_{21} \leftarrow {}^1 3_{31}$ rotational line of the (070)A^{2}A$_1$ ← (000)X^{2}B$_1$ at 675.65 nm. The absorption coefficient at line center of the NH$_3$ transition was measured in separate experiments.

II. Experimental Section

The experimental apparatus used in this work was similar to that described previously[20] except two tunable external cavity diode lasers were used to simultaneously monitor the concentration of NH$_2$ and NH$_3$. Briefly, the transverse flow reaction chamber consisted of a rectangular stainless steel vessel, containing a Teflon box of dimensions 100 × 100 × 5 cm^3. Two side chambers contained White cell optics so that the probe laser radiation could be multipassed through the rectangular photolysis volume. The gases flowed continuously at total flow rates between 200 and 600 sccm, and their partial pressures determined from their measured flow rates and the total pressure. Except for NH$_3$, the flow of each gas was monitored by calibrated digital flowmeters. The gases were used without further purification. The NH$_3$ was admitted to the reaction chamber from a separate glass vacuum line from a large 20 L storage bulb with a coldfinger kept at −40 °C using a NestLab Model CB-60 CryoCool bath. This arrangement provided a small, constant flow of 0.5 to 3.0 standard cubic centimeters per minute (sccm) of NH$_3$ over the duration of an experiment. The NH$_3$ flow was measured *in situ* from the pressure rise in a calibrated volume. The gases used were supplied by AGA having the following purities: Ar, 99.995%, CF$_4$, 99.95%, N$_2$, 99.995%, and NH$_3$, 99.99%.

The photolysis laser was a Lambda Physik Compex 205 excimer laser operating at a wavelength of 193 nm. The ArF laser fluence was varied using fine mesh stainless-steel screens. The attenuation of the photolysis laser by UV absorption of NH$_3$ was directly monitored, and it was always less than 50%.

The two probe lasers were continuous-wave external-cavity diode lasers, Environmental Optical Sensors Model 2010-ECU. One laser operated in the red spectral region from 670 to 680 nm, and was used to monitor the NH$_2$ radical on the $^1 2_{21} \leftarrow {}^1 3_{31}$ rotational line of the (0,7,0)A^{2}A$_1$ ← (0,0,0)X^{2}B$_1$ electronic transition near 675.65 nm. The other laser operated in the near-infrared region from 1460 to 1520 nm and was used to monitor the NH$_3$ molecule using a rotational transition of the (1,0,1,0) ← (0,0,0,0) combination band near 1494.12 nm. Separate Burleigh SA Plus scanning Fabry−Perot spectrum analyzers with a free spectral range of 2 GHz and a finesse of 300 continuously monitored the mode quality and the frequency stability of each laser. The output beams of the probe lasers were spatially overlapped by a dichroic mirror, and separated into two beams by a beam splitter; one beam entered a Burleigh WA150 IR wavemeter, and the other passed through the reaction zone using the White cell optics. After exiting the White cell, another dichroic mirror directed each laser beam to the appropriate detector, a New Focus Model 2051 Si photodiode and a Model 2053 InGaAs photodiode. The temporal dependence of the NH$_2$ and NH$_3$ concentrations were monitored simultaneously following the photolysis laser pulse. Differential detection of the small NH$_3$ absorption signal improved the signal-to-noise for NH$_3$ detection. The incident NH$_3$ probe laser intensity was measured using a boxcar averager triggered one millisecond before the photolysis laser. The NH$_2$ absorption signal was much larger than the NH$_3$ signal, and the probe laser

intensity could be determined directly from the transient NH_2 signal using the DC mode and the pretrigger feature of the transient recorder. The NH_3 absorption signal was small and it was necessary to remove oscillations due to thermal lensing and refractive index changes in the optical elements. The probe laser was tuned to a nearby wavelength region of zero absorption, and a background trace recorded and subtracted from the signal plus background profile in the data analysis.

Initially, the data collection was done using a LeCroy Model 9410 digital scope under the control of a laboratory PC but later the data acquisition system was up-graded to a National Instruments PXI system with multiple AD, DA and high-speed digitizer boards. The temporal absorption signals were recorded using a National Instruments Model 5122 14-bit transient recorder and the data acquisition was controlled using Labview software.

III. Results and Discussion

A. Concentration Measurements of NH_3 and NH_2. The nominal bandwidth of the radiation emitted by each probe laser (full width half-maximum < 5 MHz) was much narrower than the Doppler-broadened spectral features of the probed species, X, so that the observed absorbance at frequency, ν, $A(\nu)$ is given by the Beer–Lambert law[21]

$$A(\nu) = In(I_0(\nu)/I(\nu)) = \sigma_X(\nu)l[X] \qquad (E1)$$

where $I_0(\nu)$ is the initial laser intensity, $I(\nu)$ the transmitted laser intensity, $\sigma_X(\nu)$ the absorption coefficient at ν for species X, l the path length, and [X] is the concentration of X in molecules cm^{-3}. The absorption coefficient is related to the transition line strength $j \leftarrow i$, S_{ij}, by the normalized line shape function, $g(\nu)$, $\sigma_X(\nu) = S_{ij}g(\nu)$. Under the conditions of the present experiment, $g(\nu)$ is given by a normalized Doppler profile, $g(\nu) = \sqrt{[\ln(2)/\pi]}/[\sigma_D \exp(-\ln(2)(\nu_0 - \nu)^2/\sigma_D^2)]$, where σ_D is the half-width half-maximum (HWHM) Doppler width and ν_0 is the frequency at line center.

Ammonia was detected using the largest feature in the first $\nu_1 + \nu_3$ combination band spectral region accessible with the NIR diode laser. This feature has been assigned as a blended inversion doublet $^rR_6(6)$ rotational transition and labeled line number 1101 by Lundsberg-Nielsen et al.[22] A typical wavelength scan over this spectral feature is shown in Figure 1a using a flowing NH_3/Ar gas mixture. However, the assignment of this transition is tentative. Weber et al.[23] have also used this spectral region to probe the concentration of NH_3, and have reported measurements of $\sigma_{NH_3}(\nu_0)$ for other NH_3 transitions in this region. These workers found that the assignment of some of the NH_3 transitions was inconsistent with the measurements of their temperature dependence of the absorption coefficients. We have observed a similar behavior for the NH_3 transition used in this work so that the assignment may be in error. In any case, the concentration of NH_3 was determined using an experimentally measured value for $\sigma_{NH_3}(\nu_0)$ for the transition shown in Figure 1a. These measurements were made in either static or flowing mixtures of NH_3/Ar at total pressures less than 4 Torr and partial pressures of NH_3, P_{NH_3}, between 0.06 and 0.16 Torr. Table 1 summarizes the results of these measurements.

The laser photolysis of NH_3 at 193 nm generated the NH_2 radical and an H atom.[24] The NH_2 radical temporal concentration dependence was monitored[25] on the $^12_{21} \leftarrow \, ^13_{31}$ rotational transition of the $(0,7,0)A^2A_1 \leftarrow (0,0,0)X^2B_1$ electronic transition at 675.65 nm. Figure 1b shows a wavelength scan over the spectral region around this rotational transition. As shown in Figure 1b, this spectral feature is isolated from other NH_2
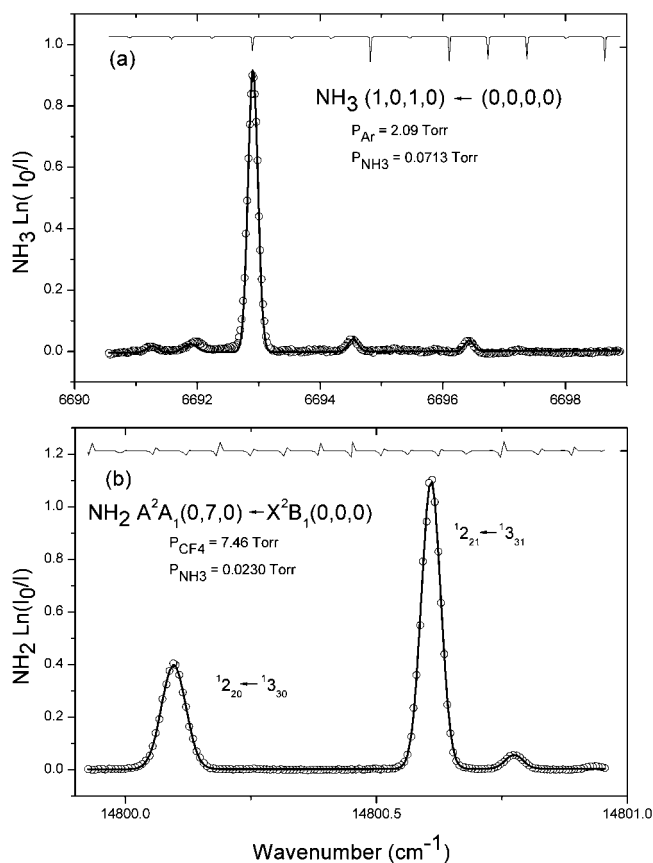
Figure 1. (a) Typical wavelength scan over the absorption feature of NH_3. The open circles (○) are the experimental points and the line is a fit to the spectrum assuming Gaussian line profiles. The upper trace is a simultaneous recording of the transmission peaks of an etalon with a FSR of 0.0645 cm^{-1}. The line width (HWHM) is 0.00940 cm^{-1}, (Doppler value 0.00995 cm^{-1}). (b) A wavelength scan over two rotational lines of the NH_2 electronic $(0,7,0)A^2A_1 \leftarrow (0,0,0)X^2B_1$ F_1 spin manifold showing that the $^12_{21} \leftarrow \, ^13_{21}$ line is well separated from other transitions in this spectral region. The open circles (○) are the experimental points and the line is a fit to the spectrum assuming Gaussian line profiles. The upper trace is a simultaneous recording of the transmission of an etalon with a FSR of 0.0647 cm^{-1}. The HWHM of the stronger absorption peak is 0.0232 cm^{-1} (Doppler value 0.0227 cm^{-1}).

TABLE 1: Summary of the Measurements of the Peak Absorption Coefficients for NH_3 and NH_2.

molecule (M)	transition	wavenumber (cm^{-1})	$\sigma_M(\nu_0)$ (cm^2 molecule^{-1})
NH_3	$(1,0,1,0) \leftarrow (0,0,0,0)$ $J'_{K'} \leftarrow J''_{K''}$ (?)	6691.83	$(1.92 \pm 0.21)^a$ $\times 10^{-19}$
NH_2	$(0,7,0)A^2A_1 \leftarrow (0,0,0)X^2B_1$ $^12_{31} \leftarrow \, ^13_{31}$	14800.59	(1.19 ± 0.18) $\times 10^{-17}$

^{a} Uncertainties: $\pm 2\sigma$ in the scatter of the data.

transitions. The peak absorption coefficient of this transition, $\sigma_{NH_2}(\nu_0)$, was determined using eq E1 after equating the initial loss of NH_3, $\Delta[NH_3]_0$, by photolysis to the initial production of NH_2, $[NH_2]_0$. The temporal absorbance profiles were extrapolated to time zero by fitting each profile to a series of exponential terms neglecting the first few 10s μs of the profile depending on the total pressure. Table 1 summarizes the results of the measurements for $\sigma_{NH_2}(\nu_0)$. The calibration procedure for the determination of $\sigma_{NH_2}(\nu_0)$ assumes that the population of both NH_3 and NH_2 have equilibrated to the bath gas temperature,

$NH_2(X^2B_1) + NH_2(X^2B_1)$ Reaction

J. Phys. Chem. A, Vol. 112, No. 51, 2008 **13435**

TABLE 2: Complete Chemical Model Describing the NH₂ + NH₂ Reaction System at 293 K

no.	reactants		products	k (cm³ molecule⁻¹ s⁻¹)^{a,b}	ref
1a	$NH_2 + NH_2$	→	$NH(X^3\Sigma^-) + NH_3$	3.0×10^{-15}	11
1b		→	$NNH_2 + H_2$		this work^c
1c		→	$N_2H_2(cis) + H_2$		
1d		→	$N_2H_2(trans) + H_2$		
1e	$NH_2 + NH_2 + M$	→	$N_2H_4 + M$	measured	this work
2a	$NH_2 + H$	→	$NH + H_2$	5.0×10^{-14}	36
2b	$NH_2 + H + M$	→	$NH_3 + M$	6.0×10^{-30} [M]^d	13
3	$NH_2 + NH$	→	$N_2H_2 + H$	1.3×10^{-10}	11
4a	$NH + NH$	→	$N_2 + 2H$	3.4×10^{-12}	37
4b		→	$NH_2 + N$	4.3×10^{-13}	38
5	$NH + H$	→	$N + H_2$	3.2×10^{-12}	39
6	$H + H + M$	→	$H_2 + M$	1.0×10^{-33}	40
7	$H + N_2H_2$	→	$H + H_2 + N_2$	3.0×10^{-13}	41
8	$H + N_2H_4$	→	$H_2 + N_2H_3$	1.5×10^{-13}	42
9	$NH_2 + N_2H_4$	→	$NH_3 + N_2H_3$	5.3×10^{-13}	43
10a	$H + N_2H_3$	→	$H_2 + N_2H_2$	1.7×10^{-11}	6
10b		→	$NH_2 + NH_2$	2.6×10^{-12}	43
11	$NH + N_2H_3$	→	$N_2H_2 + NH_2$	3.3×10^{-11}	6
12	$NH_2 + N_2H_3$	→	$N_2H_2 + NH_3$	2.8×10^{-12}	6
13	X	→	X(diffusion)	optimized	see text

^{a} Second-order rate constants units cm³ molecule⁻¹ s.⁻¹. ^{b} Third-order rate constants units cm⁶ molecule⁻² s⁻¹. ^{c} The sum of the second-order processes, $k_1^0 = k_{1a} + k_{1b} + k_{1c} + k_{1d}$. ^{d} Third body efficiency of CF₄ assumed equal to NH₃.

TABLE 3: Summary of the $\Delta H^0_f(X)$ of the Species in the NH₂ + NH₂ Reaction Model in Table 2

species	$\Delta H^0_{f, 298}(X)$ (kJ mol⁻¹)	$\Delta H^0_{f, 0}(X)$ (kJ mol⁻¹)	ref
N₂H₄	96.7 ± 4^a	111 ± 4	44
N₂H₃	225 ± 4	235 ± 4	44
NNH₂		308 ± 12^b	45
N₂H₂(cis)	201 ± 4	230 ± 4	44
N₂H₂(trans)	223 ± 4	209 ± 4	44
NH₃	-45.94 ± 0.35	-38.95 ± 0.35	46
NH₂	186.2 ± 1	189.5	47
NH	359.6 ± 0.3	359.3 ± 0.3	44, 48
N₂	0	0	
N	472.68 ± 0.4	470.8 ± 0.4	46
H₂	0	0	
H	217.998 ± 0.006	216.035 ± 0.006	46

^{a} Uncertainties in theoretical calculations taken as ± 4 kJ mol⁻¹ unless specified in the calculation. ^{b} Level of theory G3B3.

and the measured loss of each NH₃ molecule results in the production of a single NH₂ molecule.

There is evidence[26,27] that NH is formed in 193 nm photolysis of NH₃ at laser fluences greater than 3 mJ cm⁻²; however, Stephens et al.[28] could not detect NH under conditions similar to those in the present work, indicating that this yield is small. Other experiments[29,30] indicate the yield of electronically excited states of NH is also small. As will be discussed in section III.D, the rate constant measurements reported in this work were independent of ArF laser fluence varying from 1 to 30 mJ cm⁻², again implying the influence of any NH produced in the photolysis was small. Recently, we have measured[31] the yield of NH, [NH]/[NH₂], to be less than 0.002 in a CF₄ bath gas confirming that NH produced in the photolysis of NH₃ has a negligible effect in the current experiments.

The 193 nm photolysis of NH₃ does produce NH₂ with a highly excited internal energy distribution[32] and equilibration of the internal degrees of freedom of NH₂ must be complete for Equation E1 to be applicable. Fortunately, the vibrational relaxation[33] of NH₂(0,v_2,0) is rapid even in He and especially so in CF₄. Recently Yamasaki et al.[34] have measured the vibrational relaxation rate constant for NH₂(0,1,0) by CF₄ to be 3.2×10^{-11} cm³ molecule⁻¹ cm⁻³. The initial measurements

of reaction 1 were made with CF₄ as the bath gas, thus ensuring rapid equilibration of the internal degrees of both NH₂ and NH₃.

B. Reaction Mechanism. As described in recent works,[20,35] the rate constant was determined by minimizing the sum of the squares of the residuals between the observed NH₂ temporal concentration profile to one generated from a model simulation of the reaction kinetics. In order to determine the contribution a particular reaction, Y + Z, makes to the production or removal of a given species, X, the integrated reaction contribution factor, $IRCF^X_{Y+Z}$, was calculated for each species and reaction in the reaction mechanism. The $IRCF^X_{Y+Z}$ is the flux of species X that passes through reaction Y + Z, where Y or Z could be X, over a time interval t. The $IRCF^X_{Y+Z}$ was expressed as a fraction of the total concentration of species X produced or removed in the system.

Table 2 summarizes the complete reaction sequence[36-43] involving the NH₂ radical following the 193 nm laser photodissociation of NH₃, and Table 3 lists the enthalpies of formation[44-48] for each species. At 293 K, the number of reactions that contribute most to the chemistry is much smaller than the complete mechanism in Table 2. The following reactions account for almost all of the chemistry:

$$NH_3 \xrightarrow{193 \text{ nm}} NH_2^* + H$$

$$NH_2 + NH_2 \rightarrow NH(X^3\Sigma^-) + NH_3 \quad \Delta H^0_{0r} = -58 \text{ kJ mol}^{-1}$$
(1a)

$$\rightarrow NNH_2 + H_2 \quad \Delta H^0_{0r} = -70 \text{ kJ mol}^{-1} \quad (1b)$$

$$\rightarrow N_2H_2(cis) + H_2 \quad \Delta H^0_{0r} = -148 \text{ kJ mol}^{-1} \quad (1c)$$

$$\rightarrow N_2H_2(trans) + H_2 \quad \Delta H^0_{0r} = -170 \text{ kJ mol}^{-1} \quad (1d)$$

$$\xrightarrow{[M]} N_2H_4 + M \quad \Delta H^0_{0r} = -267 \text{ kJ mol}^{-1} \quad (1e)$$

$$NH_2 + H \rightarrow NH(3\Sigma^-) + H_2 \quad \Delta H^0_{0r} = -46 \text{ kJ mol}^{-1} \quad (2a)$$

$$\overset{M}{\longrightarrow} NH_3 + M \quad \Delta H^0_{0r} = -444.1 \text{ kJ mol}^{-1} \quad (2b)$$

$$NH_2 + NH \rightarrow N_2H_2 + H \quad \Delta H^0_{0r} = -124 \text{ kJ mol}^{-1} \quad (3)$$
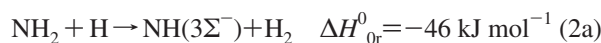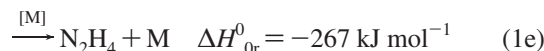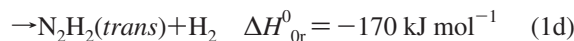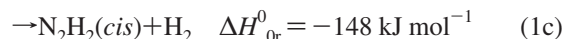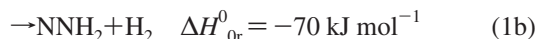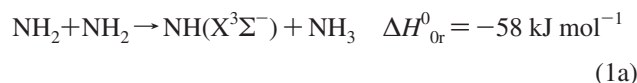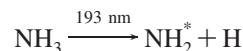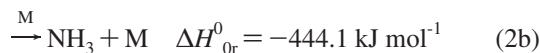
$$X \rightarrow \text{diffusion} \quad (13)$$

In fact, reactions 1a and 13, the loss of NH_2 by diffusion, make the largest contribution to the reactive flux of NH_2 in the system. It is important to be aware that many of the rate constants for the reactions in Table 2 are from theoretical calculations or extrapolations from high temperature model simulations, and have not been determined experimentally at 293 K. Reaction 1a has been discussed in the introduction and makes a negligible contribution to k_1. Dransfeld et al.[11] have made the only measurement of k_3. If there was a significant source of $NH(X^3\Sigma^-)$ in the system, reaction 3 could contribute significantly to the initial removal of NH_2, perturbing the determination of $[NH_2]_0$. As noted in the previous section, the photolysis of NH_3 was not a significant source of NH; thus, the only source of NH was reaction 2a. However, k_{2a} used in the model simulations was too small to be significant. There are no experimental measurements of k_{2a} at 300 K. The value in Table 2 was taken from a high-level theoretical calculation of Linder et al.[36] for the temperature range 500 to 3000 K. The theoretical calculated rate constants agreed with available high temperature measurements in both the forward[7] and reverse[49] directions; as well, they included tunneling effects important at low temperatures. The high temperature results of Davidson et al.[7] gives k_3 equal to 1.3×10^{-13} cm^3 molecule^{-1} s^{-1} at 293 K, but this value only results in few percent increase in the loss of NH_2 by reaction 2a. There have been no measurements of k_{2b} with CF_4 as a collision partner and only a few measurements in other bath gases, but even at the highest pressures used in this work reaction 2b only contributed a few percent to the production of NH_3. The rate constant estimates for the other reactions in the detailed mechanism listed in Table 2 were taken from extrapolations of rate constant expressions from Konnov
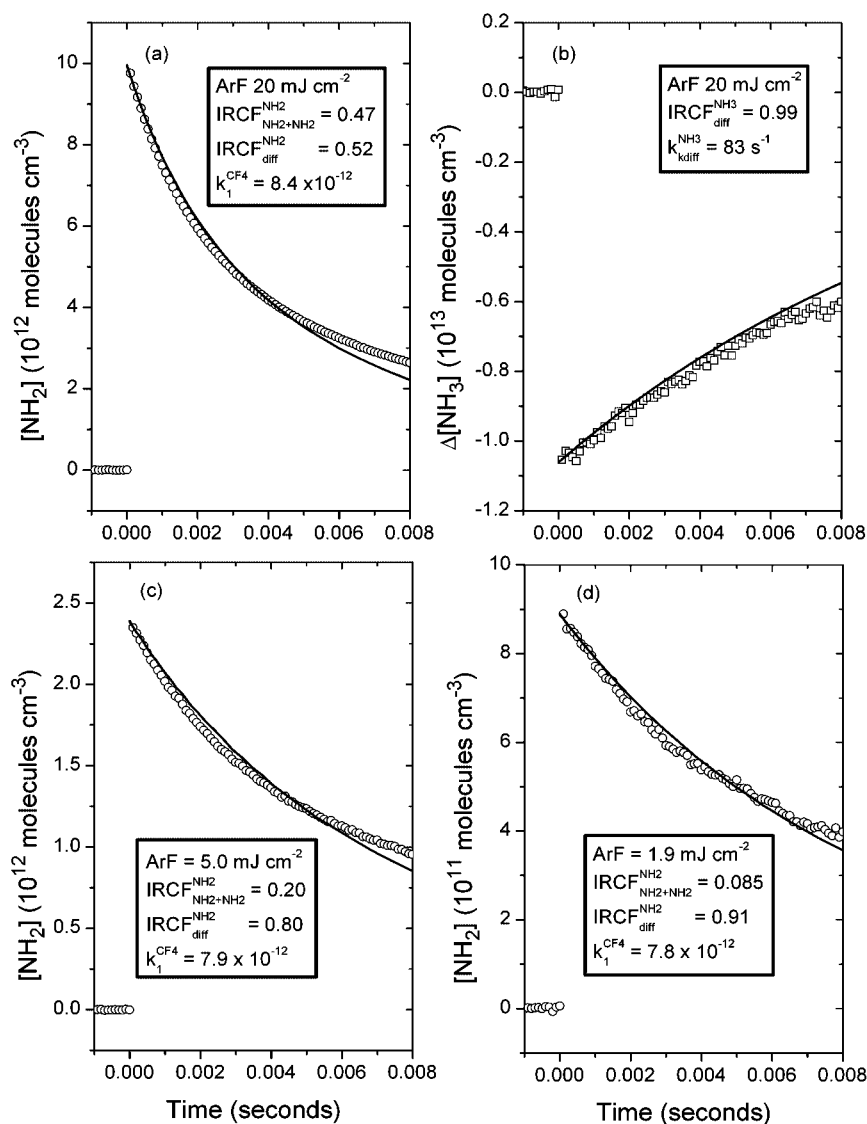
Figure 2. Determination of k_{diff}^{NH3} and k_1 at P_{CF4} = 2.433 and P_{NH3} = 0.0052 Torr and 292 K. All four panels were obtained under the same experimental conditions except different ArF laser fluences, as indicated. (a) The temporal concentration profile of NH_2 is shown. The open circles (○) are the experimental data shown every 10th data point and the solid curve is the model fit to the data. The contributions due to reaction 1a and diffusion are indicated by the ICRF$_{Y+Z}^X$ fractions in the legend. (b) The temporal concentration profile of NH_3 recorded on the same ArF laser pulse as the NH_2 profile in panel (a). The open squares (□) are the data shown every 10th point, and the solid line is the diffusion rate constant describing the replenishment of NH_3 from the surrounding gas. (c) Same as panel a except for an ArF laser fluence of 5.0 mJ cm^{-2}. (d) Same as panel a except the ArF laser fluence was 1.9 mJ cm^{-2}.

NH$_2$(X^{2}B$_1$) + NH$_2$(X^{2}B$_1$) Reaction

J. Phys. Chem. A, Vol. 112, No. 51, 2008 **13437**
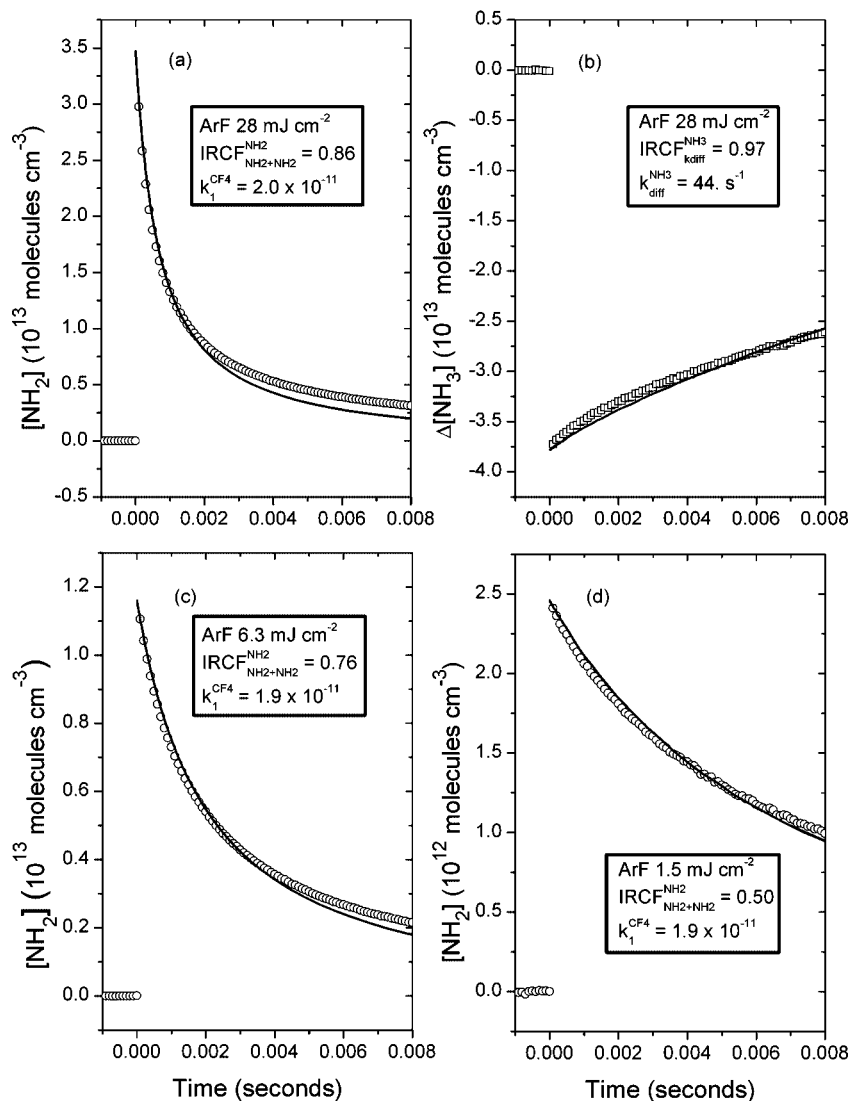
Figure 3. Similar to Figure 2 except at P_{CF4} = 6.57 and P_{NH3} = 0.0093 Torr and 293 K. The influence of diffusion is reduced compared to reaction 1a. The figure shows that k_1 is independent of the nominal ArF laser fluence and hence NH concentration. (a) Temporal dependence of NH$_2$ similar to Figure 2a. (b) Temporal dependence of NH$_3$ similar to Figure 2b. (c) Same as part a except the ArF laser fluence was reduced to 6.3 mJ cm^{-2}. (d) Same as part a except the ArF laser fluence was reduced to 1.5 mJ cm^{-2}. Note, for panel d, $k_{NH2+NH2}^{NH2}$ = 0.50 and reaction 1a and diffusion made similar contributions to the removal of NH$_2$.

and Ruyck[5,6] based on model simulations of NH$_3$ and N$_2$H$_4$ high temperature pyrolysis and combustion processes.

Diffusion is an important removal process for many species in the reaction mechanism. As discussed in recent work,[50] the diffusional loss process for each species was treated as a first-order removal process with a rate constant, k_{diff}^X = Geom D_{12}^X, where Geom is a geometrical factor and D_{12}^X is a binary diffusion constant for species X. The binary diffusion constants were calculated using the procedure of Fuller et al.,[51] and the Geom factor was determined from the measured k_{diff}^{NH3} and calculated D_{12}^{NH3}. The value of D_{12}^H was taken from the experimental measurements of Lynch and Michael.[52] As noted above, reaction 2b was the only reaction that contributed to the production or removal of NH$_3$ so that diffusion of NH$_3$ from the region outside the photolysis region was the only significant process that contributed to the replenishment of the NH$_3$ concentration. The geometry of the reaction chamber and photolysis zone produced a diffusion process that should be described by two modes of diffusion, with fast and slow exponential time constants. However, to facilitate the description of the diffusion process in the numerical simulation of the experiment, it was necessary

to make the approximation of a single exponential decay term and to limit the time interval of the simulation to 8 ms.

C. Determination of k_1. Typical NH$_2$ temporal concentration profiles are shown in Figure 2 at a low total pressure of 2.4 Torr of CF$_4$ and in Figure 3 at a higher pressure of 6.6 Torr. Figure 2b shows the NH$_3$ temporal concentration profile recorded on the same photolysis laser pulse as the NH$_2$ profile shown in Figure 2a. As mentioned in section III.A, the initial decrease in NH$_3$ concentration was used to calculate $\sigma_{NH2}(\nu_0)$ for the NH$_2$ transition. Similarly, Figure 3b shows the NH$_3$ concentration profile recorded simultaneously with the NH$_2$ profile shown in Figure 3a. The computer generated NH$_2$ concentration profiles for the optimum determination of k_1 are shown as the solid lines in Figures 2 and 3. The deviation between the experimental and computer generated profile at long times is due to the use of a single exponential decay rate constant to describe the diffusional loss process used in the model simulations, as discussed in section III.B.

Initially, k_{diff}^{NH2} was taken to be equal to k_{diff}^{NH3}; however, at low initial concentrations of NH$_2$ and especially at low pressures, 2−4 Torr, the values of k_1 were scattered and larger than

TABLE 4: Summary of Experimental Conditions and Measurements of k_1 in CF_4 at 293 ± 2 K

partial pressure (Torr)		range $[NH_2]_0$ (10^{13} molecules cm^{-3})	$k_1 \times P_{CF4}$ (10^{-11} cm^3 molecule^{-1} s^{-1} Torr^{-1})
P_{CF4}	P_{NH3}		
9.89	0.0065	0.28–1.20[a]	2.86 (± 0.20)[b]
9.11	0.0065	0.28–1.09	2.21 (± 0.14)
8.02	0.0066	0.32–1.38	1.80 (± 0.13)
7.99	0.0065	0.27–1.23	2.34 (± 0.38)
7.69	0.0099	0.55–2.46	1.86 (± 0.15)
7.50	0.0044	0.32–1.35	2.04 (± 0.12)
7.49	0.0096	0.55–2.45	1.59 (± 0.21)
6.97	0.0063	0.33–1.86	2.09 (± 0.16)
6.87	0.0066	0.33–1.39	1.82 (± 0.075)
6.57	0.0093	0.28–4.11	2.03 (± 0.15)
5.52	0.0094	0.28–2.16	1.63 (± 0.30)
4.81	0.066	0.33–1.39	1.23 (± 0.079)
4.39	0.010	0.59–3.8	1.24 (± 0.14)
3.98	0.0065	0.12–1.2	1.03 (± 0.36)
3.91	0.0066	0.33–1.39	1.02 (± 0.14)
3.25	0.0062	0.63–2.7	0.918 (± 0.13)
2.53	0.0067	0.094–1.32	0.656 (± 0.26)
2.50	0.0055	0.40–3.31	0.819 (± 0.26)
2.44	0.0052	0.21–1.06	0.813 (± 0.091)
2.10	0.0053	0.23–1.07	0.639 (± 0.18)
2.08	0.0058	0.45–2.33	0.491 (± 0.42)

[a] Multiple rate constant measurements were made with the same flow conditions. [b] Uncertainty is $\pm 2\sigma$ in the scatter of the data.

measurements at higher NH_2 concentrations for the same flow conditions. Reaction 1a is a second-order rate process so that as the concentration of NH_2 decreases, over a fixed time interval t, the flux of NH_2 radicals removed in reaction 1 also decreases, and first-order rate processes dominate the radical removal because the rate of the first-order process is independent of the instantaneous radical concentration. Diffusion is the only first-order removal process for NH_2, as shown in Table 2. At pressures near 2 Torr and small initial NH_2 concentrations, diffusion can account for more than 90% of the removal flux of NH_2, as indicated in Figure 2d by the value of $IRCF_{diff}^{NH2}$; however a single combination of k_1 and k_{diff}^{NH2} values describes the system. By varying the initial concentration of NH_2 by attenuating the photolysis laser intensity, under the same flow conditions, the relative contribution of reaction 1a and diffusion to the removal of NH_2 can be varied and the optimum combination of k_1 and k_{diff}^{NH2} determined. The following procedure for determining this optimum combination of k_1 and k_{diff}^{NH2} was adopted. For each initial NH_2 concentration, the value of k_1 that provided the best fit to the NH_2 profile was determined for a fixed value of k_{diff}^{NH2}, starting at $k_{diff}^{NH2} = k_{diff}^{NH3}$. The value of k_{diff}^{NH2} was incremented and the calculation repeated for the optimum value of k_1. As the initial NH_2 concentration decreased, the slope of a plot of k_1 against k_{diff}^{NH2} became increasingly more negative because of the larger contribution by diffusion to NH_2 removal flux at smaller concentrations. Generally, four to five initial NH_2 concentrations were analyzed at each flow condition. The region in (k_1, k_{diff}^{NH2}) coordinate space where all the plots of k_1 vs k_{diff}^{NH2} intersected or nearly so defined the best combination of k_1 and k_{diff}^{NH2} values that fit all the experimental profiles for that flow condition. The value of k_{diff}^{NH2} was found to be $(1.37 \pm 0.1) \times k_{diff}^{NH3}$, where the scatter is $\pm$ two standard deviations, $\pm 2\sigma$. At higher pressures, the contribution of diffusion to NH_2 removal becomes less significant, even at small initial NH_2 concentrations, as seen by comparing the $IRCF_{diff}^{NH2}$ in Figures 2d and 3d. At pressures greater than 4 Torr, k_{diff}^{NH2} was still assumed to be $1.37 \times k_{diff}^{NH3}$.

The experimental data for the determination of k_1 with CF_4 as third body are summarized in Table 4. The measurements of k_1 were made at a temperature of 293 ± 2 K. The third column in Table 4 lists the range of initial NH_2 concentrations achieved by attenuating the photolysis laser intensity for fixed flow conditions. The value of k_1 reported in the last column of Table 4 was the average of all the data recorded at that flow of reagents. Generally, determinations of k_1 were made for at least three different initial NH_2 concentrations, and then repeating the measurements.

Figure 4 shows typical NH_2 concentration profiles with Ar as the bath gas for a similar total pressure as in Figure 3. Parts a and b of Figure 4 were obtained in NH_3/Ar mixtures, and were recorded simultaneously. These figures illustrate the large nonequilibrium population distributions in both the NH_2 and NH_3 population manifolds. The initial portion of both profiles is shown every data point, at 10 μs interval, for the first 500 μs. The initial loss of NH_3 concentration and its rapid recovery was unexpected. One possible explanation is the repopulation of vibrational energy levels of ground-state NH_3 from fluorescence or collisional quenching of the predissociative $NH_3(A^1A_2)$ electronically excited state. With the addition of a small amount of CF_4 ($P_{CF4} = 0.121$ Torr), Figure 4c, the induction time was reduced dramatically to 30 μs, and with the further addition of CF_4 ($P_{CF4} = 0.439$ Torr), Figure 4d, was almost eliminated. The NH_3 profiles (not shown) recorded along with the NH_2 profiles in Figure 4, parts c and d, showed an even more dramatic reduction in the initial NH_3 population transient. Note, in all the fits to the data, the fitting procedure did not start at time zero but was delayed an appropriate amount depending on the duration of the observed induction time. As indicated in the labels in Figure 4, the measured value of k_1 was independent of CF_4 concentration strongly indicating that the internal degrees of freedom in NH_2 had equilibrated after an appropriate delay. The measurements in N_2 were made in a similar fashion to those in Ar. Similar to Table 4 for CF_4, the conditions of the experiment and the results of the measurement for k_1 are summarized in Table 5 and Table 6 for Ar and N_2 as carrier gas, respectively.

The overall rate constant for reaction 1 is composed of a pressure independent, $k_1^0 = \sum_{i=a}^d k_{1i}$, and a pressure dependent term, $k_{1e}[M]$, so that $k_1 = k_1^0 + k_{1e,0}[M]$. A plot of k_1 against third body concentration yields a straight line of intercept equal to k_1^0 and slope equal to $k_{1e,0}$. At the low pressures used in the experiment, reaction 1e is close to the three-body recombination pressure regime, and k_{1e} is almost a linear function of pressure. In general, the observed rate constant for a radical recombination rate constant, k, over an extended pressure range is expressed as

$$k = \frac{k_0[M]k_\infty}{k_0[M] + k_\infty} F_{cent} \qquad (E2)$$

where k_0 and k_∞ are the low-pressure recombination and high pressure second-order rate constants, respectively, and F_{cent} is a falloff broadening parameter.[53]

Parts a–c of Figure 5 show the plots of k_1 as a function of carrier gas pressure in CF_4, Ar, and N_2, respectively. In parts b and c of Figure 5, the contribution from the small partial pressure of CF_4 has been subtracted. In each figure, the solid line is a linear least-squares fit to the data for the respective collision partner, and the dashed line is a fit to the same data using eqn E2 with the parameters summarized in the figure caption. The high-pressure limiting rate constant and F_{cent} were taken from the analysis of Fageström et al.,[17] discussed below. As can be

$NH_2(X^2B_1) + NH_2(X^2B_1)$ Reaction

J. Phys. Chem. A, Vol. 112, No. 51, 2008 **13439**
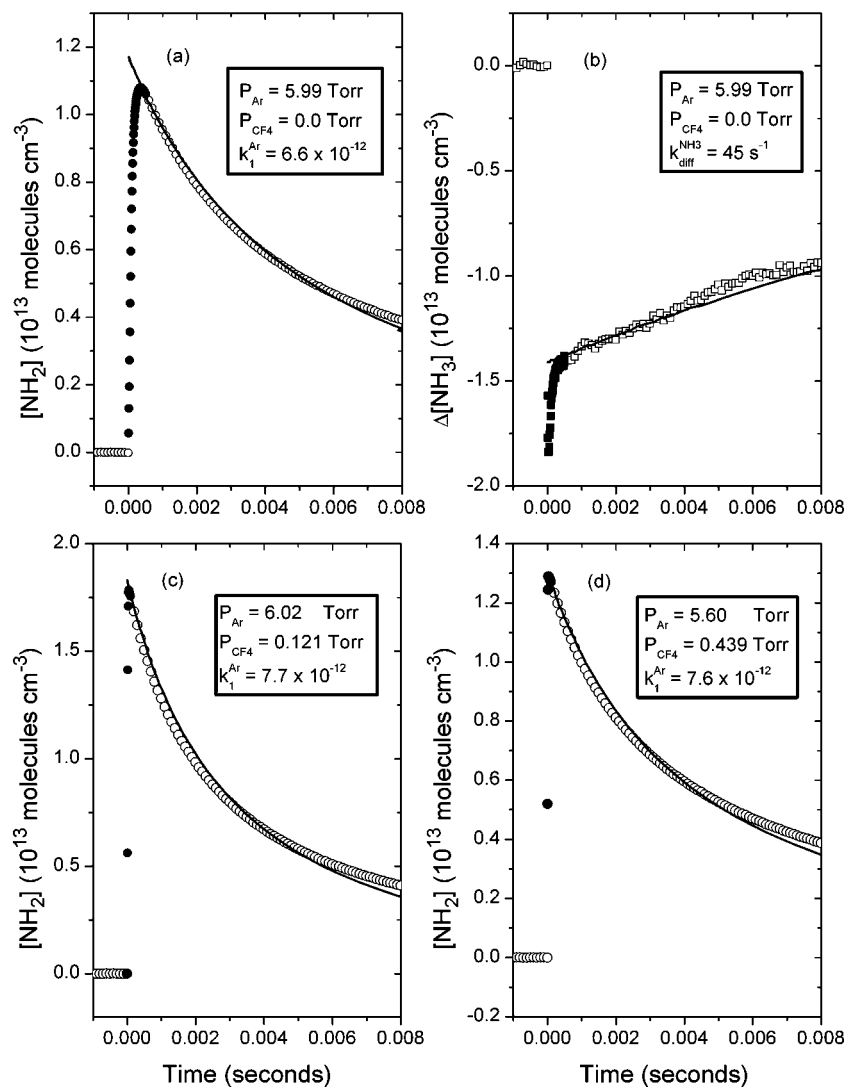
Figure 4. Influence of P_{CF4} on the determination of k_1 in Ar. (a) The temporal concentration profile of NH_2 is shown with no CF4. The $P_{AR} = 5.99$ and $P_{NH3} = 0.0067$ Torr. The ArF laser fluence was 10 mJ cm^{-2}. The data points are shown every point (●), at 10 μs intervals, for the first 500 μs and every 10th data point (○) for the rest of the profile. The solid line is the model fit to the data giving $k_1 = 6.6 \times 10^{-12}$ cm^3 molecule^{-1} s^{-1}. (b) The temporal concentration profile of NH_3 recorded simultaneously with the NH_2 trace in panel a. The data points are shown every point (■), 10 μs, and every 10th point (□), as in panel a. The transient perturbation in the NH_3 internal state distribution is of similar duration as the one for NH_2 in panel a. (c) Similar to (a) except $P_{AR} = 6.02$, $P_{CF4} = 0.121$, $P_{NH3} = 0.0055$ Torr and only the first 100 μs are shown every data point. The ArF laser fluence was 12 mJ cm^{-2}. (d) Similar to part c, except $P_{AR} = 5.60$, $P_{CF4} = 0.439$, and $P_{NH3} = 0.0055$ Torr. The ArF laser fluence was 12 mJ cm^{-2}.

seen from the Figure 5, within the scatter of the data, the rate constants are linear functions of pressure; however, as evidenced by the dashed line fit to the data in CF4, Figure 5a, k_1 has a more complicated pressure dependence than linear. A detailed master equation treatment of the data is not warranted at this time due to the scatter in the data and the uncertainty in $k_{1e,\infty}$, as will be discussed in the next section. The intercepts of the plots provide an estimate of the sum of the two-body rate constants, k_1^0, and the slope the determination of the three-body recombination rate constant for each bath gas, $k_{1e,0}$. The measurements of k_1^0 and $k_{1e,0}$ for each carrier gas are summarized in Table 7 along with a comparison to previous measurements.

D. Comparison with Previous Work. As mentioned in the Introduction, reaction 1a has been studied under a variety of conditions over the last several decades with some uncertainty among the various investigators about the value of $k_{1e\infty}$. Fagerström et al.[17] have reconciled some of the available data by combining their own measurements with those in the literature to construct theoretical falloff curves based on Troe's

and co-workers'[18,54] description of the falloff kinetics. This analysis requires the calculation of a strong collision low-pressure limiting rate constant, $k_{1rec,0}^{SC}$, the determination of the collisional efficiency factor, β_c, to calculate the low-pressure rate constant, $k_{1rec,0} = \beta_c k_{1rec,0}^{SC}$, and the calculation of the high-pressure limiting rate constant, $k_{1rec,\infty}$. An important parameter in this analysis is α, an interpolation "looseness" parameter describing the transition state for the recombination process. Fagerström et al.[17]'s analysis yielded the ratio α/β equal to 0.65, where β ($\beta = 1.89$ Å^{-1}) is the Morse potential distance parameter describing the chemical bond between the radicals. This value for α/β is larger than the average value found in the systematic investigated by Cobos and Troe,[55] comparing similar calculations to experimental falloff cures for a variety of systems. The parameters that described the system were as follows: $k_{1rec,\infty} = 1.2 \times 10^{-10}$ cm^3 molecule^{-1} s^{-1}, $\beta_c = 0.0458$, 0.112, 0.0222, and 0.0396 for SF6, NH3, Ar, and N2, respectively, and the $k_{1rec,0}$ for each collision partner listed in the Table 7. As can be seen from Table 7, the measurements of $k_{1rec,0}$ for

TABLE 5: Summary of the Experimental Conditions and Measurements of k_1 in Ar at 293 ± 2 K

partial pressure (Torr)			range of $[NH_2]_0$ (10^{13} molecules cm^{-3})	$k_1^0 + k_{1e,0}^{Ar}P_{Ar} + k_{1e,0}^{CF4}P_{CF4}$ (10^{-11} cm^3 molecule^{-1} s^{-1} Torr^{-1})
P_{Ar}	P_{CF4}	P_{NH3}		
9.35	0.454	0.0066	0.36–1.61[a]	1.29 (±0.18)[b]
8.53	0.454	0.0066	0.36–1.66	1.33 (±0.26)
7.70	0.439	0.0067	0.36–1.80	1.22 (±0.25)
6.74	0.286	0.0095	0.47–3.50	0.814 (±0.18)
6.59	0.437	0.0067	0.38–0.825	0.901 (±0.18)
6.57	0.422	0.0095	0.73–2.74	1.06 (±0.22)
6.02	0.121	0.0055	0.49–2.10	0.750 (±0.13)
5.90	0.245	0.0055	0.49–1.89	0.744 (±0.11)
5.78	0.375	0.0055	0.43–1.87	0.698 (±0.17)
5.60	0.439	0.0067	0.35–1.49	0.827 (±0.13)
4.55	0.437	0.0067	0.36–1.52	0.701 (±0.25)
3.82	0.133	0.0059	0.55–2.44	0.385 (±0.11)
3.77	0.190	0.0060	0.56–1.18	0.409 (±0.13)
3.63	0.433	0.0067	0.31–1.65	0.544 (±0.067)
3.48	0.422	0.0061	0.55–2.34	0.495 (±0.058)
2.80	0.433	0.0066	0.35–1.52	0.448 (±0.035)
2.72	0.215	0.0070	0.51–0.73	0.317 (±0.080)
9.75	0.0	0.0066	0.32–1.35	1.19 (±0.14)
9.05	0.0	0.0067	0.68–0.85	0.963 (±0.17)
7.99	0.0	0.0067	0.35–1.57	0.963 (±0.17)
7.00	0.0	0.0067	0.34–1.42	0.794 (±0.11)
6.77	0.0	0.0091	0.27–3.12	0.622 (±0.22)
6.15	0.0	0.0054	0.48–2.00	0.584 (±0.12)
5.99	0.0	0.0063	0.30–1.29	0.664 (±0.11)
4.03	00.	0.0067	0.30–1.39	0.510 (±0.089)

[a] Multiple rate constant measurements were made with the same flow conditions. [b] Uncertainty is ± 2σ in the scatter of the data.

TABLE 6: Summary of the Experimental Conditions and Measurements of k_1 in N_2 at 293 ± 2 K

partial pressure (Torr)			range of $[NH_2]_0$ (10^{13} molecules cm^{-3})	$k_1^0 + k_{1e,0}^{N2}P_{N2} + k_{1e,0}^{CF4}P_{CF4}$ (10^{-11} cm^3 molecule^{-1} s^{-1} Torr^{-1})
P_{N2}	P_{CF4}	P_{NH3}		
9.76	0.448	0.0067	0.35–1.45[a]	2.09 (±0.081)[b]
9.39	0.433	0.0065	0.37–1.72	1.99 (±0.07)
8.25	0.441	0.0066	0.36–1.72	1.97 (±0.21)
6.99	0.428	0.0066	0.66–1.58	1.54 (±0.12)
6.54	0.423	0.0065	0.81–1.63	1.54 (±0.098)
6.02	0.432	0.0066	0.72–1.67	1.43 (±0.15)
5.50	0.432	0.0066	0.70–1.49	1.48 (±0.069)
4.59	0.411	0.0064	0.76–0.95	1.07 (±0.13)
3.80	0.406	0.0063	0.66–0.83	0.921 (±0.12)
3.55	0.396	0.0061	0.61–1.37	0.966 (±0.12)
9.65	0.0	0.0067	0.45–1.81	1.68 (±0.14)
8.66	0.0	0.0067	0.46–1.85	1.52 (±0.24)
7.99	0.0	0.0067	0.41–1.85	1.48 (±0.24)
6.93	0.0	0.0067	0.41–1.79	1.08 (±0.072)
5.97	0.0	0.0066	0.44–1.85	0.880 (±0.12)
4.98	0.0	0.0066	0.44–1.87	0.694 (±0.15)
3.99	0.0	0.0066	0.44–1.83	0.581 (±0.085)

[a] Multiple rate constant measurements were made with the same flow conditions. [b] Uncertainty ±2σ in the scatter of the data.

Ar and N_2 reported in the present work are about a factor of 5 larger than those determined by Fagerström et al.,[17] although the relative efficiency for these two collision partners agree within experimental error. The experimental measurements of Khe et al.[14] for N_2 and Ar as third bodies are about a factor of 2 smaller than those found in the analysis of Fagerström et al.[17] Thus, the difference between the measurements of the present work and the previous experimental measurement of $k_{1rec,0}$ is even larger than suggested by the summary in Table 7.

As just noted, prior to the work Fagerström et al.[17] the determinations of $k_{1rec,\infty}$ were scattered, ranging from 2.5×10^{-11} to 1.3×10^{-10} cm^3 molecule^{-1} s,$^{-1}$ illustrating the difficulty in determining accurate rate constants for radical–radical reactions and especially determining the high-pressure limiting rate constant. Previous studies of reaction 1a used a variety of

techniques to initiate the reaction: pulse radiolysis,[13,17] flash photolysis,[14,15] or laser initiated reaction,[16] and a variety of methods to monitor the temporal concentration of the NH_2 radical: white light absorption spectrophotometry,[13,14,17] intra-cavity laser absorption,[15] or high-resolution laser absorption spectroscopy,[16] all using rotational lines of the $(0,9,0)A^2A_1 \leftarrow (0,0,0)X^2B_1$ vibronic band. The experimental challenge is to convert the observed NH_2 absorption signals into absolute concentration measurements. In all cases, this was done in an indirect manner and by necessity in separate experiments. In the current work, these problems were over come by directly observing the temporal NH_2 concentration profile according to eq E1 and monitoring directly the initial loss of NH_3 and the production of NH_2 simultaneously on the same excimer laser pulse. Furthermore, there was no ambiguity in defining the

NH$_2$(X^{2}B$_1$) + NH$_2$(X^{2}B$_1$) Reaction

J. Phys. Chem. A, Vol. 112, No. 51, 2008 **13441**

TABLE 7: Comparison of k$_1$ Determined in This Work and Previous Measurements at 293 K

carrier gas	k_1^0 (10^{-13} cm^3 molecule^{-1} s^{-1})	$k_{1e,0}$ (10^{-29} cm^6 molecule^{-2} s^{-1})	ref
CF$_4$	6.2 ± 8.8[a]	8.04 ± 0.46	this work
SF$_6$		2.0 ± 0.41	17
NH$_3$		5.2 ± 2.2	17
N$_2$	3.9 ± 1.6	5.7 ± 0.7	this work
		1.4 ± 0.58	17
Ar	0 ± 7.5	3.94 ± 0.37	this work
		0.70 ± 0.30	17
NH$_3$/N$_2$/Ar	14		14
He	13 ± 5		19

[a] Uncertainties ±2σ in the of scatter of the data

optical path length through the photolysis region: it was completely defined by the distance between the UV−IR dichroic mirror and the ZnS plate placed on the optical axis of the white cell.

Figure 6 compares the measurements of k$_{1e}$ made in the present work in N$_2$, Figure 6a, and Ar, Figure 6b, as collision partners to the available data for these two systems over the complete experimental pressure range. The results of the theoretical Troe analysis for k_{1e}^{N2} and k_{1e}^{Ar} performed by Fagerström et al.,[17] as just discussed, are shown by the solid lines in Figures 6a and 6b. The dashed lines in Figure 6 are the predicted falloff rate constants calculated using the values for $k_{1e,0}^{N2}$ and $k_{1e,0}^{Ar}$ listed in Table 7 instead of those used in the Troe fit to the data by Fagerström et al.[17] It is clear from Figure 6 that the results of the present work differ from previous low-pressure measurements by a factor of 10. However, the revised falloff curves, calculated using the experimentally determined $k_{1e,0}^{N2}$ and $k_{1e,0}^{Ar}$ values, predict high-pressure rate constants that are within a factor of 2 of the measurements of Lozovskii et al.[15] for the respective third body. Using the results of Fagerström et al.[17] and the values of $k_{1e,0}^{N2}$ and $k_{1e,0}^{Ar}$ measured in this work, new values of β_c were calculated to be 0.17 and 0.11 for N$_2$ and Ar, respectively, and are closer to expectations[53] for β_c than the original estimates of Fagerström et al.[17]

The determinations of the total disproportionation reaction rate constant, k_1^0, determined in the present and previous work are also included in Table 7. Khe et al.[14] measured k_1^0 in the same manner as determined here, and obtained the same intercept in each carrier gas they examined, NH$_3$, N$_2$, and Ar. As noted above, their measurement of $k_{1rec,0}$, in Ar and N$_2$ is almost a factor of 8 smaller than measured here, see Table 7 and the previous paragraph. The average of the values for the three gases examined in the present work gives $k_1^0 = (3.4 ± 6) × 10^{-13}$ cm^3 molecule^{-1} s^{-1}. Although these measurements probably agree within the experimental scatter, it is not clear how to compare the two measurements in light of the large discrepancy between the k$_{1rec,0}$ determinations. A more direct measurement of k_1^0 is provided by the work of Stothard et al.,[19] also included in Table 7 and discussed in the introduction. These measurements were made at He pressures of 0.53 and 0.75 Torr, and guided by the results of Khe et al.[14] for $k_{1e,0}$ in Ar, the recombination reaction in He was assumed negligible. However, using the results reported here for $k_{1rec,0}$ in Ar and accounting for the reduced collisional efficiency of He compared to Ar, 50%, the recombination reaction would still contribute over 30% to the measured decay of NH$_2$ in their experiments. If the measurements of the present work are correct, the measurements of k_1^0 by Stothard et al.[19] have over estimated k_1^0, in closer agreement to the value of k_1^0 determined in the present work.
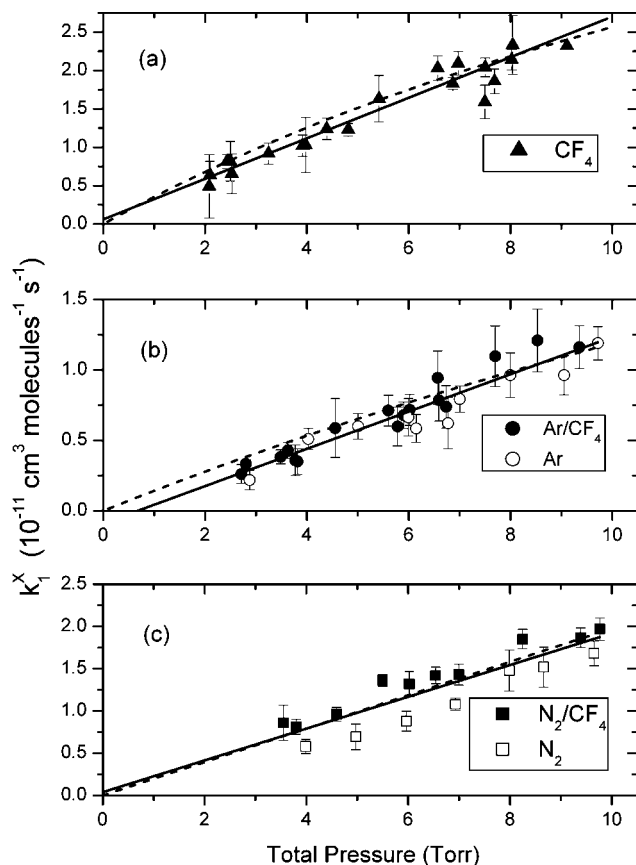
Figure 5. Summary of the pressure dependence of k_1. The experimental data are summarized in Tables 4, 5, and 6 and the values of the slopes and intercepts from the least-squares fits in the figures are given in Table 7. (a) CF$_4$ as the third body (▲). The error bars are the scatter in the data at the ± 2σ level of confidence from at least six independent measurements. The solid line is a least-squares fit to the data. The dashed line is k$_{1e}$ given by eq E2 with $k_{1e0}^{CF4} = 1.6 × 10^{-28}$ cm^6 molecule^{-2} s^{-1}, $k_{1e∞} = 1.2 × 10^{-10}$ cm^3 molecule^{-1} s^{-1} and $F_{cent} = 0.7$. (b) Similar to (a) only Ar as the third body. The open circles, (○), were measurements of k_1 in NH$_3$/Ar mixtures and the solid circles, (•), were made with small amounts of CF$_4$ added. The dashed line is k$_{1e}$ given by eq E2 with $k_{1e0}^{Ar} = 8.0 × 10^{-29}$ cm^6 molecule^{-2} s^{-1}, $k_{1e∞} = 1.2 × 10^{-10}$ cm^3 molecule^{-1} s^{-1} and $F_{cent} = 0.55$. (c) Similar to (b) except N$_2$ is the third body. The open squares, (□), were measurements of k_1 in NH$_3$/N$_2$ mixtures and the solid squares (■) were made with small amounts of CF$_4$ added. The dashed line is k$_{1e}$ given by eq E2 with $k_{1e0}^{N2} = 1.0 × 10^{-28}$ cm^6 molecule^{-2} s^{-1}, $k_{1e∞} = 1.2 × 10^{-10}$ cm^3 molecule^{-1} s^{-1} and $F_{cent} = 0.6$.

E. Estimated Uncertainty in k_1. As indicated in Figures 2, 3, and 4, the model simulations of the experimental profiles included the calculation of IRCFs for each reaction in Table 2, and showed that reaction 1 and k_{diff}^{NH2} accounted for over 95% of the removal of NH$_2$ while reaction 2a accounted for most of the remainder. The scatter in the data for k_1 reported in Tables 4, 5, and 6 resulted in the average of the values of k_1 obtained under varying initial concentrations of NH$_2$ but under the same flow conditions, and hence, reflects the influence of both k_{diff}^{NH2} and k_1. The scatter in the determination of k_{diff}^{NH2} was ± 7.5% at the 2σ level of confidence as discussed in Section III C. The average uncertainty in scatter of the measurements of k_1 summarized in Tables 4, 5, and 6 was taken to be ± 17% so that the combined uncertainty from the model simulations was ±19%, assuming the uncertainties are uncorrelated.

The determination of k_1 requires knowledge of the NH$_2$ concentration. The largest contributor to the uncertainty in the determination of $\sigma_{NH2}(\nu_0)$ was tuning the NH$_3$ probe laser
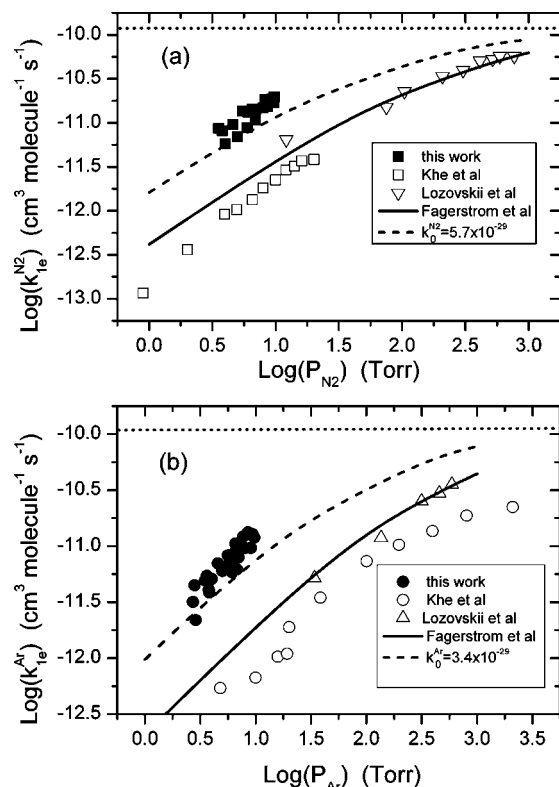
Figure 6. (a). Comparison of the results of this work with previous experimental data for reaction 1e with N_2 as a third body. The symbols are: filled squares (■), this work, open squares (□), ref 14, and right side up triangle (△), ref 15. The solid line (—) is the result of the Troe analysis by Fagerström et al.[17] for k_{1e} based on eq E2. The dotted horizontal line references the value of $k_{1e, \infty}$ determined by Fagerström et al. The dashed line (- - -) is the same Troe analysis except $k_{1e, 0}$ for N_2 given in Table 7 was used instead of the value determined by Fagerström et al. (b) Similar to part a, except Ar is the third body. The symbols are as follows: filled circles (●) this work, open circles (○), ref 14, and upside down triangle (▽), ref 15. The lines are the same as in part a, except the $k_{1e, 0}$ from Table 7 for Ar was used in the Troe analysis.

frequency to the peak of the weak NH_3 absorption feature. Although boxcar averaging enhanced the signal-to-noise of the NH_3 absorption signal, noise due to pulse-to-pulse fluctuations of the excimer laser intensity could not be completely suppressed. The NH_2 absorption signal was calibrated assuming that the initial loss of NH_3 resulted in the initial production of NH_2. Combining the uncertainties in the determination of the NH_3 and NH_2 absorption coefficients summarized in Table 1 gives the total uncertainty in the determination of the NH_2 concentration as $\pm$ 19%, at the $\pm 2\sigma$ confidence level.

Other possible influences on the determination of rate constants for second-order rate process have been discussed in a recent work.[20] As a precaution, the partial pressure of NH_3 was always small so that the excimer laser attenuation was never more than 50%. This also reduces the possibility of distortions in the NH_3 concentration distribution along the photolysis axis due to saturation effects of the photolysis laser intensity.[56]

Uncertainties in path length and pressure measurements were less than a few percent and did not contribute significantly to the total uncertainty dominated by the scatter in the data, the determination of k_{diff}^{NH2} and the uncertainty in the NH_2 concentration. Combining these three uncertainties gives a total uncertainty in the measurement of k_1 of ± 27%, including systematic and random errors at the $\pm 2\sigma$ level of confidence.

IV. Summary

The rate constant measurements for reaction 1 exhibited a linear dependence on pressure, Figure 5, with slopes determined to be 8.0×10^{-29} in CF_4, 5.7×10^{-29} in N_2, and 3.9×10^{-29} cm^6 molecule^{-2} s^{-1} in Ar. The uncertainty in these rate constant measurements was estimated to be ± 27%, including random and systematic errors. The reaction was initiated by 193 nm laser photolysis of flowing dilute NH_3 mixtures in the carrier gas. The measurements were made by simultaneously monitoring NH_3 and NH_2 temporal concentration profiles using time-resolved high-resolution absorption spectroscopy. These measurements are a factor of 8 larger than previous determinations[14,17] of these rate constants, as summarized in Table 7. The average intercept of the linear plots of k_1 as a function of pressure of the carrier gas represents k_1^0, and was found to be $(3.4 \pm 6) \times 10^{-13}$ cm^3 molecule^{-1} s^{-1}, where the uncertainty is the scatter in the data at the 2σ level of confidence. This measurement is almost a factor of 4 smaller than several previous determinations[14,19] but within the scatter of the experimental measurements.

References and Notes

(1) Miller, J. A.; Bowman, C. T. *Prog. Energy Combust.* **1989**, *15*, 287.

(2) Huges, K. J.; Tomlin, A. S.; Hampartsoumian, E.; Nimmo, W.; Zsély, I. G.; Ujvári, M.; Turányi, T.; Clague, A. R.; Pilling, M. J. *Combust. Flame* **2001**, *124*, 573.

(3) Gardiner, W. C., Jr. *Gas-Phase Combustion Chemistry*; Springer-Verlag: New York, 1999.

(4) Zabetta, E. C.; Hupa, M. *Combust. Flame* **2008**, *152*, 14.

(5) Konnov, A. A.; Ruyck, J. D. *Combust. Sci. Technol.* **2000**, *152*, 23.

(6) Konnov, A. A.; Ruyck, J. D. *Combust. Flame* **2001**, *124*, 106.

(7) Davidson, D. F.; Kohse-Höinghaus, K.; Chang, A. Y.; Hanson, R. K *Int. J. Chem. Kinet.* **1990**, *22*, 513.

(8) Allen, M. T.; Yetter, R. A.; Dryer, F. L. *Combust. Flame* **1998**, *112*, 302.

(9) Skreiberg, Ø.; Kilpinen, P.; Glarborg, P. *Combust. Flame* **2004**, *136*, 501.

(10) Dentener, F. J.; Crutzen, P. J. *J. Atmos. Chem.* **1994**, *19*, 331.

(11) Dransfeld, P.; Hack, H.; Kurzke, H.; Temps, F.; Wagner, H. GG. *Twentieth Symposium (International) on Combustion*; The Combustion Institute: Pittsburgh, PA 1984; p 655.

(12) Xu, Z.-F.; Fang, D.-C.; Fu, X.-Y *Int. J. Quantum Chem.* **1998**, *70*, 321.

(13) Gordon, S.; Mulac, W.; Nangia, P. *J. Phys. Chem.* **1971**, *75*, 2087.

(14) Khe, P. V.; Soullgnac, J. C.; Lesclaux, R. *J. Phys. Chem.* **1977**, *81*, 210.

(15) Lozovskii, V. A.; Nadtochenko, V. A.; Sarkisov, O. M.; Cheskis, S. G. *Kinet. Katal.* **1979**, *20*, 111.

(16) Patrick, R.; Golden, D. M. *J. Phys. Chem.* **1984**, *88*, 491.

(17) Fagerström, K.; Jodkowski, J. T.; Lund, A.; Ratajczak, E. *Chem. Phys. Lett.* **1995**, *236*, 103.

(18) Troe, J. *J. Phys. Chem.* **1979**, *83*, 114.

(19) Stothard, N.; Humpfer, R.; Grotheer, H.-H. *Chem. Phys. Lett.* **1995**, *240*, 474.

(20) Bahng, M.-K.; Macdonald, R. G. *J. Phys. Chem. A* **2007**, *111*, 3850.

(21) Kroto, H. W. *Molecular Rotational Spectra*; Dover: New York, 1992.

(22) Lundsberg-Nielsen, L.; Hegelund, F.; Nicolaisen, F. M. *J. Mol. Spectrosc.* **1993**, *162*, 230.

(23) Webber, M. E.; Baer, D. S.; Hanson, R. K. *Appl. Opt.* **2001**, *40*, 2031.

(24) Okabe, H.; *Photochemistry of Small Molecules*; Wiley Interscience; New York, 1978.

(25) Ross, S. C.; Birss, F. W.; Vervloet, M.; Ramsay, D. A. *J. Mol. Spectrosc.* **1988**, *129*, 436.

NH$_2$(X^{2}B$_1$) + NH$_2$(X^{2}B$_1$) Reaction

J. Phys. Chem. A, Vol. 112, No. 51, 2008 **13443**

(26) Donelly, V. M.; Baronavski, A. P.; McDonald, J. R. *Chem. Phys.* **1979**, *43*, 283.

(27) Wolf, M.; Yang, D. L.; Durant, *J. Phys. Chem. A* **1997**, *101*, 6243.

(28) Stephens, J. W.; Morter, C. L.; Farhat, S. K.; Glass, P. G.; Curl, R. F. *J. Phys. Chem.* **1993**, *97*, 8944.

(29) Kenner, R. D.; Rohrer, F.; Stuhl, F. *J. Chem. Phys.* **1987**, *86*, 2036.

(30) Kenner, R. D.; Rohrer, F.; Browarzik, R. K.; Kaes, A.; Stuhl, F. *Chem. Phys.* **1987**, *118*, 141.

(31) Bahng, M.-K.; Macdonald, R. G. Manuscript in preparation.

(32) Loomis, R. A.; Reid, J. P.; Leone, S. R. *J. Chem. Phys.* **2000**, *112*, 658.

(33) Yamasaki, K.; Watanabe, A.; Kakuda, T.; Itakura, A.; Fukushima, H.; Endo, M.; Maruyama, C.; Tokue, I. *J. Phys. Chem. A* **2002**, *106*, 7728.

(34) Yamasaki, K.; Watanabe, A.; Tanaka, A.; Sato, M.; Tokue, I. *J.Phys. Chem. A* **2002**, *106*, 6563.

(35) Gao, Y; Macdonald, R. G *J. Chem. Phys. A* **2005**, *109*, 5388.

(36) Linder, D. P.; Duan, X.; Page, M. *J. Phys. Chem.* **1995**, *99*, 11458.

(37) Nicholas, J. E.; Spiers, A. I.; Martin, N. A. *Plasma Chem. Plasma Proc.* **1986**, *6*, 39.

(38) Xu, Z.-F.; Fang, D.-C.; Fu, X.-Y. *Chem. Phys. Lett.* **1997**, *275*, 386.

(39) Adam, L.; Hack, W.; Zhu, H.; Qu, Z.-W.; Schinke, R. *J. Chem. Phys.* **2005**, *122*, 11430.

(40) Baulch, D. L.; Cobos, C. J.; Cox, R. A.; Esser, C.; Frank, P.; Just, Th.; Kerr, J. A.; Pilling, M. J.; Troe, J.; Walker, R. W.; Warnatz, J. *J. Phys. Chem. Ref. Data* **1992**, *21*, 411.

(41) Linder, D. P.; Duan, X.; Page, M. *J. Chem. Phys.* **1996**, *104*, 6298.

(42) Vaghjiani, G. L *Int. J. Chem. Kinet.* **1995**, *27*, 777.

(43) Gehring, V. M.; Hoyermann, K.; Wagner, H. Gg.; Wolfrum, J. *Ber. Bunsenges. Phys. Chem.* **1971**, *75*, 1287.

(44) Matus, M. H.; Arduengo, A. J., III; Dixon, D. A *J. Phys. Chem. A* **2006**, *110*, 10116.

(45) Harding, L. H. Private communication.

(46) Cox, J. D.; Wagman, D. D.; Medvedev, V. A. *CODATA Key Values for Thermodynamics*; Hemisphere: New York, 1989.

(47) Rusic, B.; Boggs, J. E.; Burcat, A.; Csásáz r, A. G.; Demaison, J.; Janoschek, R.; Martin, J. M. L.; Morton, M. L.; Rossi, M. J.; Stanton, J. F.; Szalay, P. G.; Westmoreland, P. R.; Zabel, F.; Bérces, T *J. Phys. Chem. Ref. Data* **2005**, *34*, 573.

(48) Dixon, D. A.; Feller, D.; Peterson, K. A. *J. Chem. Phys.* **2001**, *115*, 2576.

(49) Rohrig, M.; Wagner, H. Gg. *Twenty-Fifth Symposium (International) on Combustion*; The Combustion Institute: Pittsburgh, PA, 1994; p 975.

(50) Gao, Y.; Macdonald, R. G *J. Phys. Chem. A* **2006**, *110*, 977.

(51) Fuller, E. N.; Ensley, K; Giddings, J. C. *J. Phys. Chem.* **1969**, *73*, 3679.

(52) Lynch, K. P.; Michael, J. V *Int. J. Chem. Kinet.* **1978**, *10*, 233.

(53) Holbrok, K. A.; Piling, M. J.; Robertson, S. H. *Unimolecular Reactions*; Wiley: Chichester, U.K., 1996.

(54) Gilbert, R. G.; Luther, K.; Troe, J. *Ber. Bunsen-Ges. Physik. Chem.* **1983**, *87*, 169.

(55) Cobos, C. J.; Troe, J. *J. Chem. Phys.* **1985**, *83*, 1010.

(56) Davidson, D. F.; Chang, A. Y.; Hanson, R. K. *Twenty-Second Symposium (International)*; The Combustion Institute: Pittsburgh, PA, 1988; p 1877.